

<https://doi.org/10.1038/s42005-025-02021-4>

Data-driven picosecond X-ray imaging for quantitative plasma-induced shock characterization

Check for updates

Christopher S. Campbell¹✉, Mirza Akhter², Samuel Clark³, Kamel Fezzaa³, David Staack² & Zhehui Wang¹✉

Imaging dynamic events, especially shockwave behavior, is key to advancing high-energy-density (HED) research. Recent advances in fourth- and fifth-generation X-ray light sources allow for high-resolution imaging of fast phenomena, but limited beam time necessitates maximizing data acquisition. We present a benchtop-scale pulsed plasma device submerged in liquid heptane, capable of generating dynamic events at rates exceeding 10 Hz, supporting the field's data-driven goals by producing large, high-quality imaging datasets. Using X-ray phase contrast imaging (XPCI) at the Advanced Photon Source, we imaged weak shockwaves (Mach ~ 1.2) in heptane interacting with plasma-induced cavitation bubbles, causing deviation from Rankine-Hugoniot behavior; to our knowledge, this represents the first direct imaging of such interaction. Our quantitative analysis offers insight into weak shock phenomena and energy-focusing applications in pulsed plasmas. These results highlight the potential for large datasets to advance dynamic HED research at current light source facilities, and have implications for fields such as inertial confinement fusion, plasma-enhanced chemical processing, and biomedical applications.

After over two centuries since the development of the first camera, direct imaging photography has remained a valuable and data-rich method for exploring and understanding a wide range of physical phenomena, and in more recent decades the availability of advanced imaging methods for scientific investigation has increased drastically. A modern example of this progress is the recent emergence of fourth- and fifth-generation light sources and upgraded user facilities, such as the Advanced Photon Source (APS) at Argonne National Laboratory¹, the European Synchrotron Radiation Facility (ESRF)^{2,3}, the European XFEL⁴, the LCLS-II free-electron laser at the SLAC National Accelerator Laboratory⁵, and the National Ignition Facility (NIF) at Lawrence Livermore National Laboratory⁶ which use high resolution and brightness to interrogate extremely small and fast phenomena. However, available experiment time at these advanced light sources is quite limited^{7,8}. Efficient use of experiment time therefore relies on the ability to maximize the event repetition rate of dynamic targets, since a large amount of high-quality data typically lends itself to more nuanced scientific insights; this concept has been identified as the future of the high-energy-density (HED) plasma physics community and is encapsulated within the term data-driven⁹.

Many dynamic processes of recent interest to the HED community such as blast wave structure¹⁰, dynamic compression¹¹, and fluid breakup¹², often involve destructible devices which necessitate constant target reassembly, restricting event rates to perhaps only a few events per hour. It is therefore beneficial to develop dynamic targets which require minimal to no maintenance between events, without compromising phenomena of interest to the HED plasma physics community such as high instantaneous power density, high mass density gradients, high pressure and temperature gradients, and supersonic behavior/shockwaves^{13–20}. In particular, the dynamic interaction of travelling shockwaves with matter has been a subject of significant interest and study in recent decades, for example the study of high-temperature high-pressure responses of materials^{21,22}, shock-shock interaction phenomena^{23,24}, the design of shock-resistant materials^{25,26}, and in inertial confinement fusion (ICF)²⁷. Typically, these phenomena are investigated at high event repetition rates via laser-based energy deposition^{9,28}, however these laser systems tend to be cost-prohibitive and relatively immobile, therefore not conducive for a single research group to use at different light facilities.

In this work, we present the development and implementation of a benchtop-scale pulsed plasma device submerged in liquid heptane, designed

¹P-4 Thermonuclear Plasma Physics, Los Alamos National Laboratory (LANL), Los Alamos, NM, 87545, USA. ²Plasma Engineering and Non-equilibrium Processing Laboratory, Department of Mechanical Engineering, Texas A&M University (TAMU), College Station, TX, 77843, USA. ³X-ray Science Division, Advanced Photon Source, Argonne National Laboratory (ANL), Argonne, IL, 60439, USA. ✉e-mail: christopher.campbell@lanl.gov; zwang@lanl.gov

to generate reproducible HED dynamic events at repetition rates exceeding 10 Hz (an event rate of high interest to HED physics). Utilizing X-ray phase contrast imaging (XPCI) at Argonne’s APS, we capture high-resolution images of the device’s plasma-driven shockwaves with an unprecedented sensitivity to weak shocks (Mach ~ 1.2), with imaging exposure times of ~ 50 ps at 6.5 MHz frame rates. This work demonstrates the capability of high-repetition-rate, non-laser-driven HED experiments to enhance data availability, improve imaging sensitivity, and facilitate quantitative analysis. Similarity of this work to the submerged exploding wire XPCI experiments by Yanuka²⁹ at the ESRF allows for direct comparison of these two XPCI implementations for similar imaging targets; for Yanuka, peak instantaneous power and total event energy were approximately 1 GW and 300 J, respectively (recall 1 MW and 100 mJ for this work). The fact that the shock front images presented in this work are still visible at such small event energies highlights the superior sensitivity and utility of XPCI as a diagnostic for analyzing lower-energy shocks, facilitating methods of analysis which can draw more subtle quantitative data directly out of these images. This work also shares conceptual similarities with XPCI shock imaging by Barbato³⁰ at Germany’s Petawatt High-Energy Laser for Heavy Ion EXperiments (PHELIX), but distinguishes itself through a higher imaging frame rate and the incorporation of multiple physics-based analyses. These analyses reveal deviations from the standard Rankine-Hugoniot shock behavior, which we attribute to interactions between the propagating shock front and the expanding cavitation bubble—an effect directly imaged and characterized here for the first time, to the best of our knowledge. The methods of quantitative thermodynamic analysis and energy balance results presented herein aid in improving understanding and control of this pulsed plasma phenomena^{31,32}, for further utilization of pulsed plasmas in fields such as chemical processing of liquids^{33,34}, non-equilibrium liquids sterilization for biomedical applications³⁵, and other plasma-enhanced engineering applications^{36,37}.

Results and discussion

Experimental setup, phase contrast imaging results

The pulsed power device and high-voltage circuit utilized in this study to generate submerged spark discharges is akin to those in our previous work^{37,38}; the implementation used in this work consists of two electrodes submerged in ambient heptane between which a well-timed spark discharge occurs using a laser-triggered voltage pulser (see Fig. 1). After charging a 1nF capacitor to 14.5 kV, corresponding with approximately 100 mJ of stored energy, the event of interest dissipates a fraction of this energy, about 70 mJ, via nanosecond-timescale plasma processes in the imaging target (light, sound, chemistry, shockwaves) over 100 ns, implying an instantaneous power of roughly 0.7 MW. Assuming an approximate discharge region diameter of 5 μm during peak current (an estimation taken from prior work which imaged pre-discharge plasma initiation channels³⁸) across a gap of 0.5 mm, we estimate a peak surface power density of 3.6 TW/cm² and a peak energy density of 7.3 TJ/m³, which falls within the regime relevant to HED physics (> 100 GJ/m³³⁹).

For this work, the target was taken to the Argonne National Laboratory’s APS synchrotron for ultrafast XPCI experiments. The X-ray imaging method for this work used a 128-frame Shimadzu HPV-X2 camera (3 μm /pixel) to image a LYSO scintillator in line with the synchrotron source and imaging target. The 6.5 MHz imaging framerate was enabled by the APS’s 24-singlet standard operating mode⁴⁰. Figure 2a shows selected XPCI frames from a single spark discharge event, while Fig. 2b compiles frames from multiple similar events, sorted by frame time relative to plasma initiation.

Shock speed over time

Figure 3 shows an estimated shock speed of 1.45 ± 0.13 km/s for this event, corresponding to a Mach number of 1.28 ± 0.12 in ambient liquid heptane ($v_{\text{sound}} = 1.129$ km/s). The shock images’ transverse XPCI profiles are consistent with what is expected for a step discontinuity in density. A slight negative concavity in the data implies that the shock speed decreases with time, consistent with the time-dependent shock speed found by linearly

fitting to subsamples of this dataset (within 100 ns of a given time). Although the dimensional analysis result from Taylor-von Neumann-Sedov blast wave theory might seem applicable here (where the time-dependent shock position $R(t)$ is proportional to $t^{0.4}$ for spherically expanding shocks^{41,42} and to $t^{0.5}$ for cylindrically expanding shocks⁴³), this work’s plasma-induced shock front contradicts the theory’s two main assumptions: instantaneous energy input and negligible ambient pressure ($p_{\text{post-shock}} \gg p_{\text{ambient}}$). By the time the shock becomes visible to this diagnostic (earliest measured shock image at 45 ns after initiation), the post-shock pressure has decreased drastically, resulting in a near-linear position vs. time relation; this is consistent with O’Malley’s experimental⁴⁴ and Magaletti’s computational¹⁵ results for expanding shocks in liquids. Therefore, we deemed a phenomenological quadratic fit (Fig. 3, green curve) to be appropriate for velocity estimations in this work, as it minimizes assumptions while still exhibiting negative concavity during these timescales.

Phase contrast imaging computational model

The X-ray absorption contrast for such a weak shock is quite low; in our imaging target, absorption contrast for the shock is 0.02% (6mm path length through heptane, 100 μm shocked region, 20% density increase), well below the camera’s detectability limit. However, the edge enhancement properties of XPCI cause this shock to be visible above background noise as localized maxima and minima in brightness, with the maxima occurring on the pre-shock side of the discontinuity. This type of diffraction is the essence of XPCI and can be described by the Fresnel-Kirchhoff integral⁴⁴, modified for translationally symmetric geometries in Equation (2) to ease computation:

$$g_{\text{out}}(x', y') = \frac{e^{2\pi iz/\lambda}}{i\lambda z} \iint g_{\text{in}}(x, y) e^{\frac{i\pi}{z}(x'-x)^2 + (y'-y)^2} dx dy \quad (1)$$

$$= \frac{e^{2\pi iz/\lambda}}{\sqrt{i\lambda z}} \int g_{\text{in}}(x) e^{\frac{i\pi}{z}(x'-x)^2} dx \quad (2)$$

where g_{in} and g_{out} represent the complex-valued electric field at the target and the imaging plane respectively, λ is the X-ray wavelength being used (for X-ray energies of ~ 25 keV, $\lambda = 50$ pm; see Fig. S1 in the Supplementary Information for this work’s full X-ray spectrum), and z is the target-to-detector distance ($z = 46$ cm). All information about the target is contained in g_{in} as complex-valued index of refraction data, taken from⁴⁵; see Methods for more detail. This model can now be fit to experiment (Fig. 4, analyzing the fifth frame from Fig. 2b), establishing a measurement technique to estimate post-shock density. This density measurement method was used to analyze a subset of seven XPCI frames from multiple events featuring a visible shock image. Combining this method with knowledge of each frame’s relative delay reveals time-dependent behavior of the shock density ratio ρ_2/ρ_1 ; the observed decay of ρ_2/ρ_1 over time is determined solely from physics-based computational analysis of the XPCI images and is consistent with expanding shock front behavior (see Fig. S2 in the Supplementary Information).

Energy balance in post-shock region

Combining this density measurement capability with knowledge of electrical energy input (via simultaneous voltage and current measurement), we can describe the system’s energy balance thermodynamically. As mentioned previously, we quantify the total amount of electrical energy being exerted during the event via simultaneous measurement of voltage across and current through the imaging target, such that cumulative electrical energy input over time is calculated via $U_{\text{total}}(t) = \int_0^t P(t') dt' = \int_0^t V(t') I(t') dt'$. This event energy dissipates via several possible mechanisms in this dynamic event, such as light, sound, chemistry, and heat; for this work, we define $U_{\text{shock}}(t)$ as the cumulative excess internal energy relative to ambient at a given time within the post-shock region, which to a first-order approximation should be proportional to total energy: $U_{\text{shock}}(t) = \alpha \cdot U_{\text{total}}(t)$. By also assuming that the shock expands roughly spherically, energy density in the post shock region bounded between the

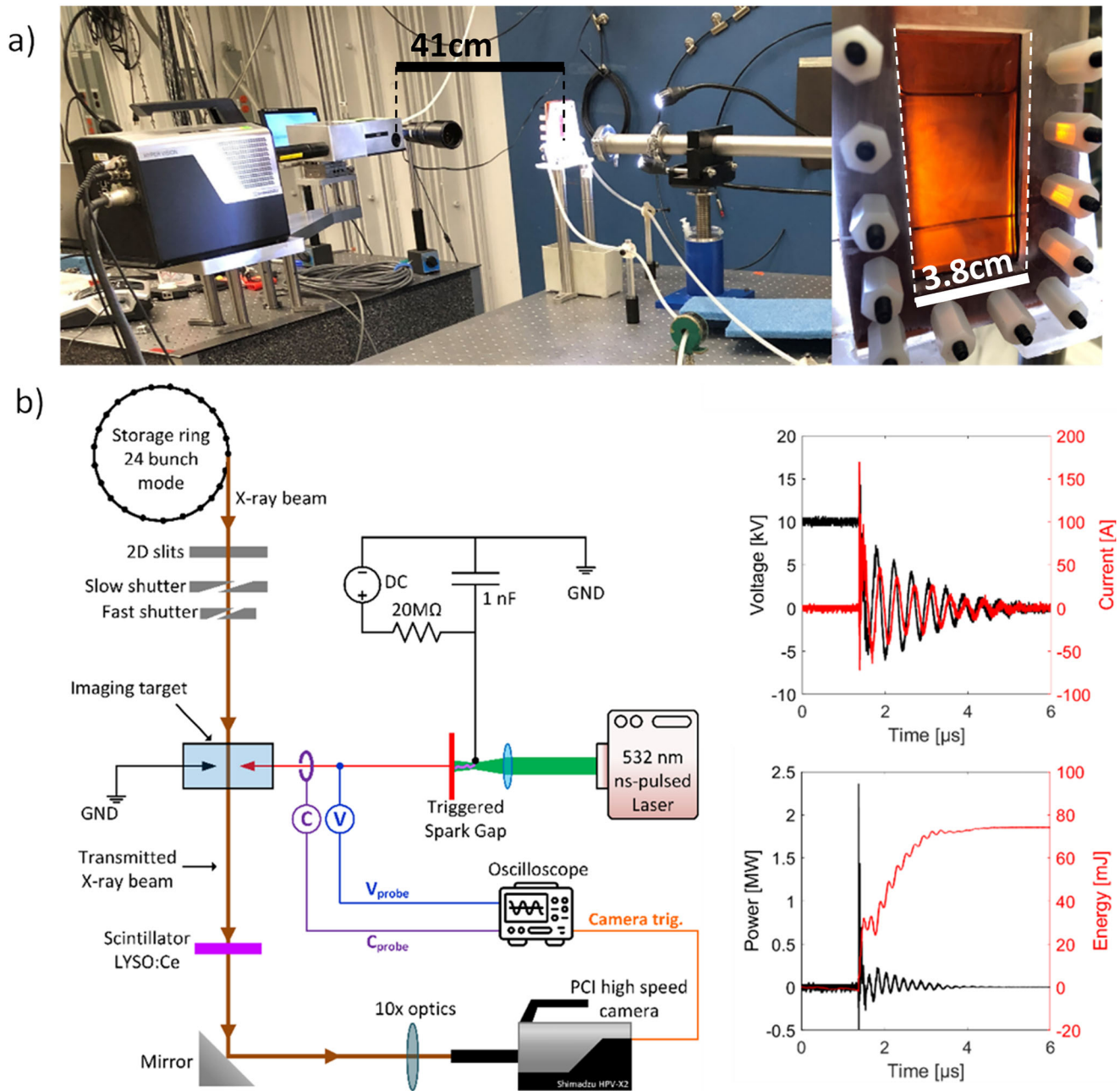


Fig. 1 | The experimental setup used in this work. **a** Photograph of the overall experimental setup. Synchrotron X-ray light enters the experiment via the light pipe on frame right, passes through the plastic imaging target (see closeup in second photograph), and into the scintillator-camera assembly on frame left. **b** Schematic of the experimental setup which shows how the synchrotron facility, plasma circuit, and scintillator-camera assembly are configured. The two plots on the right show typical electrical diagnostic results.

shock front and the cavitation bubble surface can be expressed as $\Delta u(t) = U_{\text{shock}}(t) / (\rho_2(t) \cdot \frac{4}{3}\pi \cdot (R_{\text{shock}}(t)^3 - R_{\text{bubble}}(t)^3))$, where $\Delta u(t) = u_2(t) - u_1$ is the excess specific internal energy above ambient. Combining this expression with a power law $\rho_2(t)/\rho_1 = A \cdot \Delta u(t)^B + 1$ derived from heptane's equation of state⁴⁶, we arrive at the following expression:

$$\frac{\rho_2(t)}{\rho_1} = A \cdot \left(\frac{\alpha \cdot U_{\text{total}}(t)}{\rho_2(t) \cdot \frac{4}{3}\pi \cdot (R_{\text{shock}}(t)^3 - R_{\text{bubble}}(t)^3)} \right)^B + 1 \quad (3)$$

where $A = 2.05 \times 10^{-3} \text{ kg}^B \text{ J}^{-B}$ and $B = 0.415$ are the power law parameters for heptane. $U_{\text{total}}(t)$, $R_{\text{shock}}(t)$ and $R_{\text{bubble}}(t)$ are determined directly from

electrical diagnostics and imaging data. By implicitly solving for $\rho_2(t)$ and using α as a fitting parameter, we can now include the analytical model from Equation (3), which as shown in Fig. 5a agrees well with the XPCI model results. This thermodynamic model is related to the phenomenological fit to ρ_2/ρ_1 vs. t data from diamond shock compression XPCI experiments by Schropp at SLAC's LCLS⁴⁷. A notable result of this physics-based analysis is measurement of $U_{\text{shock}}(t)$ as a fraction of $U_{\text{total}}(t)$; in this case that fraction is $\alpha = U_{\text{shock}}(t)/U_{\text{total}}(t) \sim 3\%$. This $\alpha = 3\%$ fitted model curve is shown in Fig. 5a alongside curves for $\alpha = 0.3\%$ and $\alpha = 30\%$, to illustrate the measurement sensitivity of this energy balance method; while this sensitivity appears to be relatively weak, it is indeed significant enough to reject the no-heating null hypothesis ($\alpha = 0\% \rightarrow \rho_2/\rho_1 = 1$). As mentioned in the introduction, the ability of this work's analysis to discern quantitative

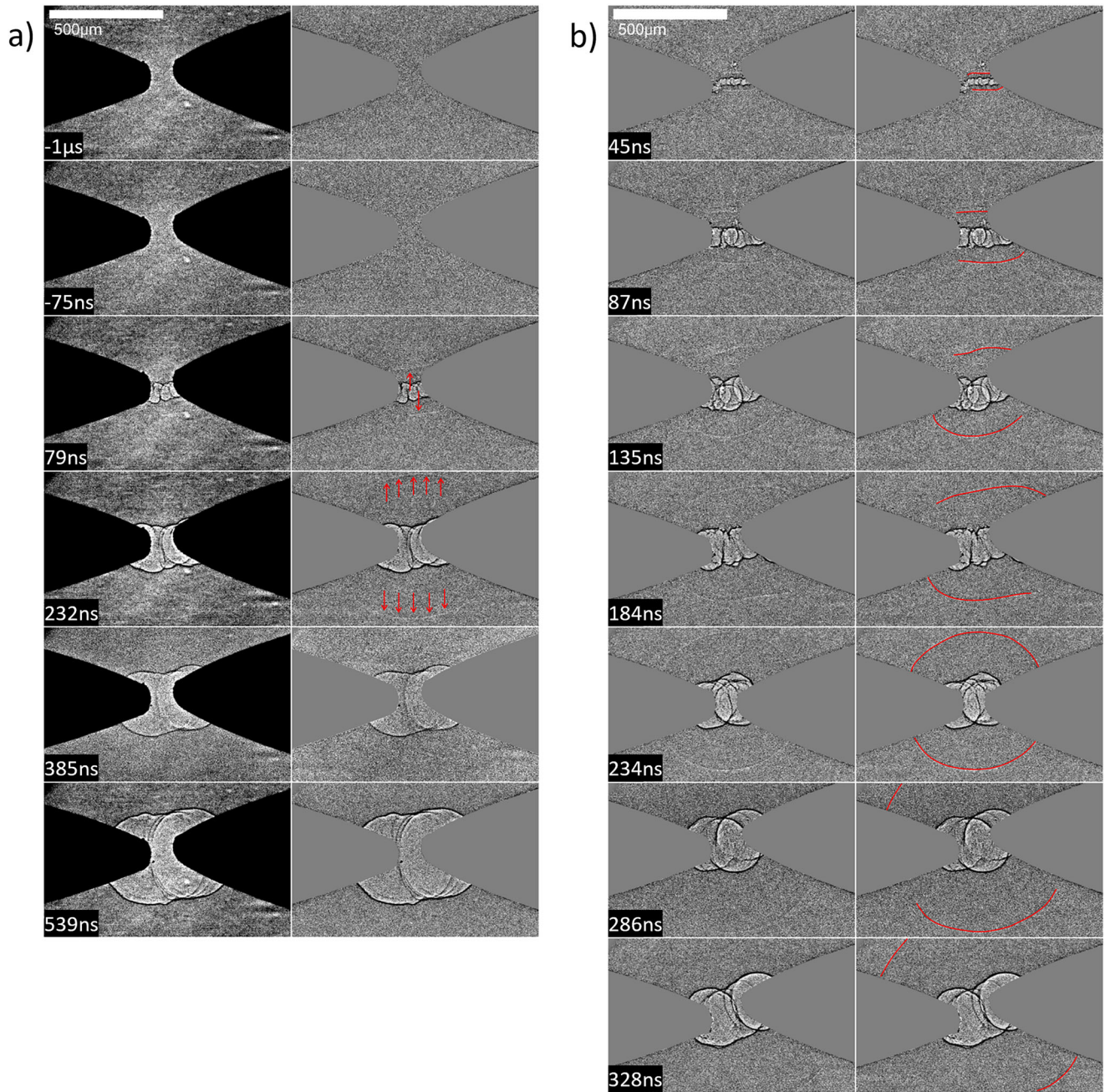


Fig. 2 | The XPCI experimental data analyzed in this work, showing plasma-induced expanding shock fronts in liquid heptane. a Selected frames from a single dynamic event, with timestamps measured relative to plasma initiation. Left and right columns show contrast-enhanced raw XPCI frames and corresponding background-subtracted frames, respectively. The interframe period is 153.4ns (6.5MHz framerate). Note the location of the shock front visible at $t = 79\text{ns}$ and $t =$

232ns, denoted by red arrows. The 500- μm scale bar applies to all frames. **b** A collection of time-sorted XPCI frames from selected events in which a shock front is visible. In this case we have duplicated each background-subtracted frame across both columns, with solid red annotations on the right column indicating the contour of the shock. The 500- μm scale bar applies to all frames.

information, such as this bounding range on α , represents a contribution to the field of XPCI analysis for dynamic events, compared with the typical extent of XPCI analysis⁴⁸.

Rankine–Hugoniot shock analysis

Alongside the X-ray diffraction model method for measuring ρ_2/ρ_1 , it is possible to relate ρ_2 and v_{shock} by solving the system of Rankine-Hugoniot thermodynamic shock relations^{49–51}, which in this case are derived from one-dimensional Rankine-Hugoniot conservation of mass, momentum, and energy between Regions 1 (the pre-shock ambient region) and 2 (the

post-shock region):

$$\begin{cases} \rho_1 v_1 = \rho_2 v_2 \\ p_1 + \rho_1 v_1^2 = p_2 + \rho_2 v_2^2 \\ h_1 + v_1^2/2 = h_2 + v_2^2/2 \end{cases} \quad (4)$$

These normal shock relations use the moving reference frame where the shock is stationary, and liquid at ambient pressure and temperature is entering the shock at velocity v_1 and exiting at v_2 . While this

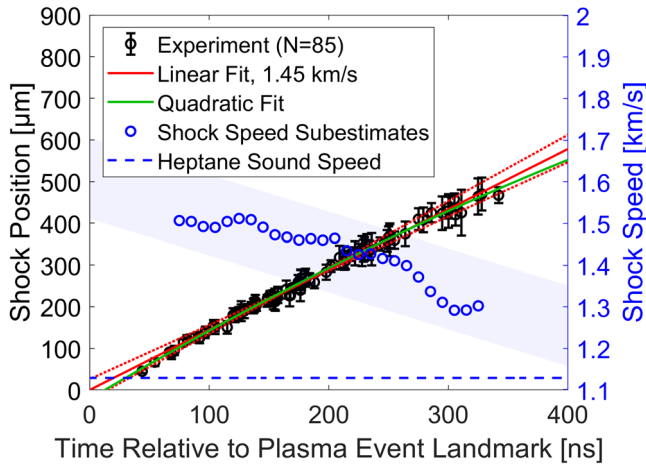


Fig. 3 | Cylindrical shock positions over time, relative to the axis of the plasma. This plot compiles data from eighty-five different XPCI frames for which the shock was visible, each of which is represented by a black circle with vertical error bars in this plot. Shock position measurement was performed manually for each of the frames, with the vertical error bars indicating two standard deviations away from the average of twenty manual position measurements taken for each frame. From electrical diagnostics, we can assign a relative timestamp (precise to < 1 ns) to each frame, hence the horizontal position of each point on this plot. Blue circles indicate shock speed subestimates calculated by fitting to subsamples of the full set of shock positions. The green curve shows a quadratic fit to the position vs. time data.

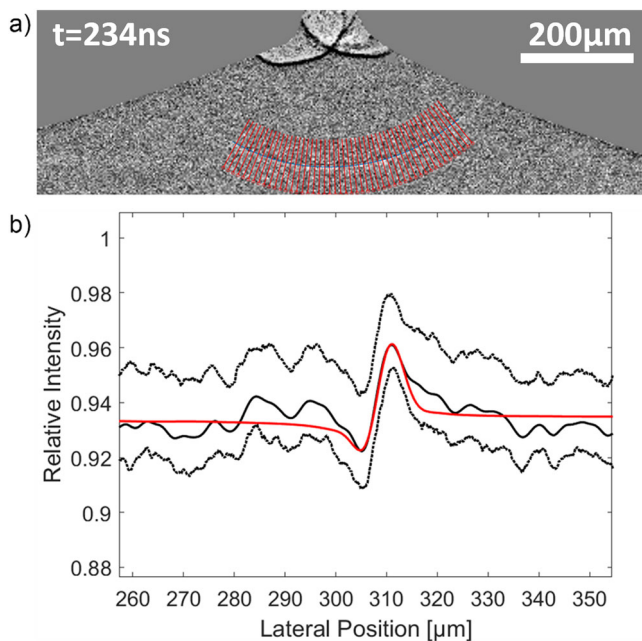


Fig. 4 | Illustration of a cutline extraction algorithm which converts the two-dimensional XPCI frame of the shock front into a one-dimensional intensity plot. **a** Example of the shock contour cutlines being extracted via a spline fit to the shock in an XPCI frame, in this case the fifth image from Fig. 2b ($t = 234$ ns). **b** By averaging together all of these extracted cutlines, we arrive at the solid black average cutline, with dotted lines showing upper and lower quartiles of this averaging. The solid red line shows the simulated XPCI shock front profile (Equation (2)) that best fits this image; in this case this method suggests a post-shock density of $\rho_2 = 0.799^{+0.116}_{-0.057} \text{ g/cc}$ ($\rho_2/\rho_1 = 1.176^{+0.171}_{-0.084}$).

one-dimensional form of Rankine-Hugoniot relations is typically used to describe planar shock fronts, the shocks imaged in this work can be considered locally normal since they are thin ($< 1 \mu\text{m}$) compared with the shock’s overall shape/curvature. In place of the gas law assumption typically

made at this point to proceed analytically, we can use thermodynamic tables for the liquid of interest to relate the thermodynamic parameters $p(t)$, $\rho(t)$, $u(t)$, and $h(t)$ of the post-shock region. This results in a closed system of equations that can be used to construct a separate ρ_2/ρ_1 vs. v_{shock} relation which can be compared with the relation from the XPCI computational model results.

After performing this comparison, XPCI-measured values for ρ_2/ρ_1 and v_{shock} (from the XPCI model and quadratic fit to Fig. 3, respectively) tend to reside above the Rankine-Hugoniot curve in Fig. 5b, suggesting a higher-density post-shock region than what is predicted by Rankine-Hugoniot alone. We attribute this to the fact that the Rankine-Hugoniot description ignores the cavitation bubble which follows the expanding shock, clearly visible in Fig. 2a, b. This bubble interface expands outward from a relatively small radius ($< 10 \mu\text{m}$) and high energy density, compressing the post-shock region to a higher density. This concept is illustrated with green asterisks in Fig. 5b, generated by assuming that this compression only affects the post-shock density without affecting the speed of the shock, and implemented by multiplying the density ratio from the original Rankine-Hugoniot relation by the compression ratio $1/(1 - (R_{\text{bubble}}/R_{\text{shock}})^2)$. Although this correction factor still does not result in a model that sufficiently matches experiment, it represents the maximum ρ_2/ρ_1 curve which could be justified by the data. Conversely, the original Rankine-Hugoniot model (sans correction factor) represents the minimum bound on ρ_2/ρ_1 , since it completely neglects this compression effect; the XPCI-measured values for ρ_2/ρ_1 in Fig. 5b are conceptually bounded by the curves made from these two extreme and opposite assumptions. The observation and quantification of the bubble-shock coupling effect shown here may inform a range of physics and engineering applications of this type of submerged plasma discharge, for example in plasma-assisted drilling³⁷, focused underwater shocks for tumor treatment³⁵, defense of naval vessels^{52,53}, amongst others^{54,55}.

In reality, the compression-induced higher ρ_2/ρ_1 should increase the shock speed, an effect not fully explored here. Full investigation of this effect should include a multiphysics model which couples together the dynamics of the cavitation bubble and liquid post-shock region (Rayleigh-Plesset, Navier-Stokes) with the shock jump conditions (Rankine-Hugoniot).

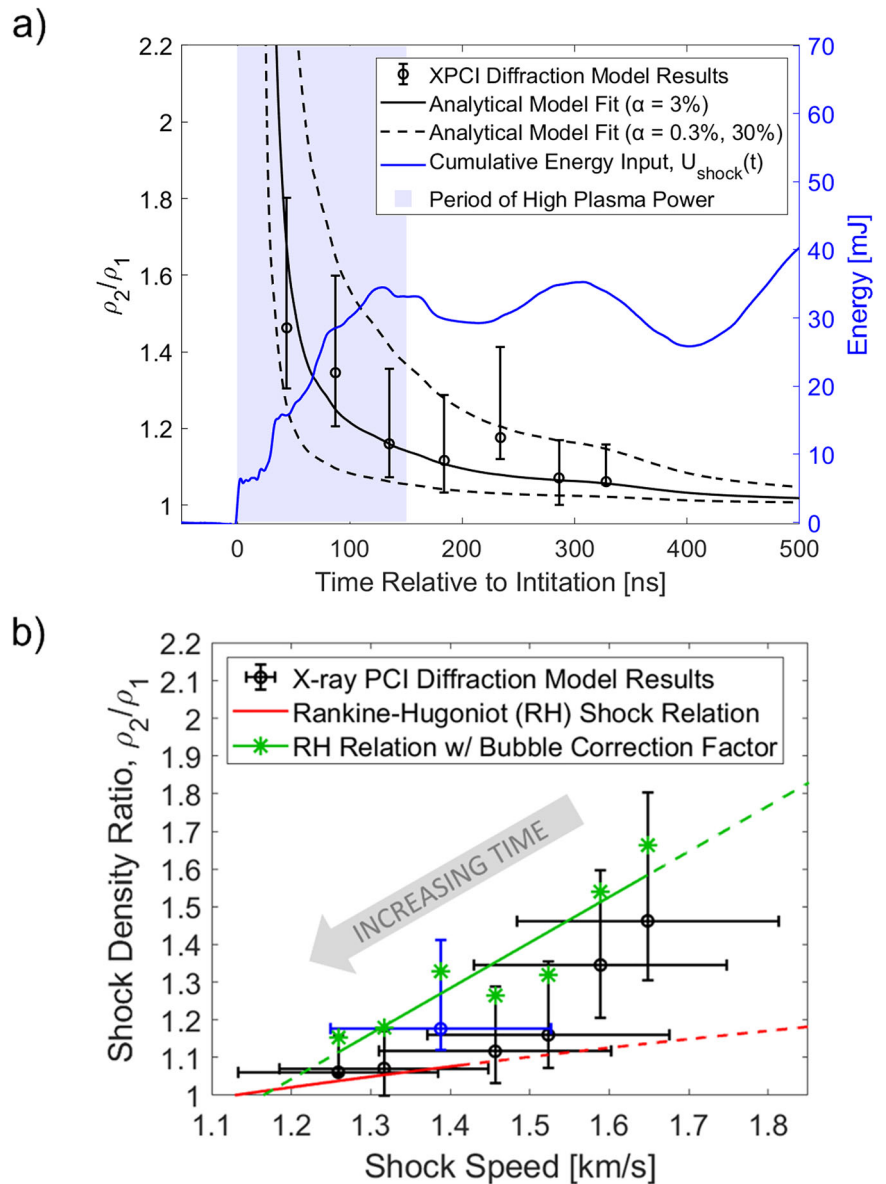
Toward quantitative analysis of longitudinal shock contour

Major quantitative analysis results of the shock discussed in this work have been limited to the lateral direction, perpendicular to the shock front. Shock profile cutlines as shown in Fig. 4 were fully averaged together and directly compared to the equivalent simulated XPCI profile. However, this overall approach to quantitative XPCI analysis is also potentially sensitive to longitudinal shock structure, information which the aforementioned outline averaging method ignores. Figure 6b illustrates this idea by plotting image brightness as a function of longitudinal and lateral position relative to the shock front.

Unfortunately, this particular method of analysis highlights one of the limitations of the XPCI dataset featured in this work. The APS X-ray source and imaging setup used in this work is known to have an elliptical instrument function which is wider in the horizontal direction; for the shock contour XPCI in this work, this anisotropic instrument function “smears” vertically oriented shock fronts more than those that are horizontally oriented. The overall result of this effect is apparent when imaging otherwise uniform spherical shock fronts, since the measured image will be blurred more on the left and right sides of the sphere than on the top and bottom, following a cosine relation with the shock contour angle (relative to horizontal). This is exactly what we see in Fig. 6c, which shows the difference in brightness between the XPCI maximum and minimum (the XPCI “prominence”) at a particular position along the shock front, with included cosine fit.

Without the effects of detector noise and source anisotropy on the XPCI data, it would be possible to extract values for ρ_2/ρ_1 for each individual position along the shock front without averaging, a feat which would have broad implications for the future of XPCI. Although such analysis is

Fig. 5 | Summary plots of the XPCI-enabled density and speed measurements performed in this work. a Decay of shock density ratio with time. This plot compiles together the simulated XPCI results which best fit experiment (black circles) as a function of time relative to plasma initiation; horizontal error bars indicate an assumed shock speed uncertainty (estimated from the parabolic fit in Fig. 3) of $\pm 10\%$, and vertical error bars indicate the range of density ratios which produce simulated XPCI shock profiles which would still fall within the upper and lower quartiles of the experimental average shock profile (Fig. 4b). By fitting the thermodynamic model from Equation (3) to these points (solid black curve), we conclude that $\alpha \sim 3\%$ of the event's total stored energy is expressed as excess internal energy behind the shock. This same model for alternate values of α are shown (dashed black curves) to roughly illustrate uncertainty. The blue curve and shaded area highlight the timescale of significant energy input to the system, as measured via electrical diagnostics. **b** Hugoniot states in the ρ_2-v_{shock} plane, showing how values estimated from this work's XPCI data and diffraction model (black) compare to normal shock thermodynamic relations in heptane both with (green) and without (red) the cavitation bubble compression effect. Vertical error bars (ρ_2/ρ_1) match those of Fig. 5a, and horizontal error bars (v_{shock}) assume a simple $\pm 10\%$ uncertainty. The blue datapoint corresponds with the X-ray diffraction model fit result from Fig. 4.



infeasible for the dataset featured in this work, this research avenue has the potential to enhance the future of quantitative and data-driven image analysis of dynamic events. Especially with the emergence of next-generation improvements such as the recently upgraded Advanced Photon Source (APS-U) as well as the ESRF, both of which have superior brightness and emittance^{1,2,56}, the ability to take full advantage of brighter and higher-quality light sources in order to perform increasingly sensitive physics-based analysis is steadily becoming more important.

Conclusion

In summary, we present robust and repeatable observations of weak shocks in liquid heptane and their interaction with the plasma-induced cavitation bubble at timescales previously obscured by optical emission. This achievement represents progress in imaging sensitivity and resolution, and advances an underexplored approach for physics-based quantitative analysis of subtle physical phenomena using XPCI. The high repetition rate (> 3 events/minute), low cost ($< \text{US}\$100\text{k}$), and portability of this imaging target make it quite attractive to those fields interested in similar dynamic events (e.g. ICF, dynamic compression, shock physics), but which rely on apparatuses which are either immovable or have a prohibitively slow event

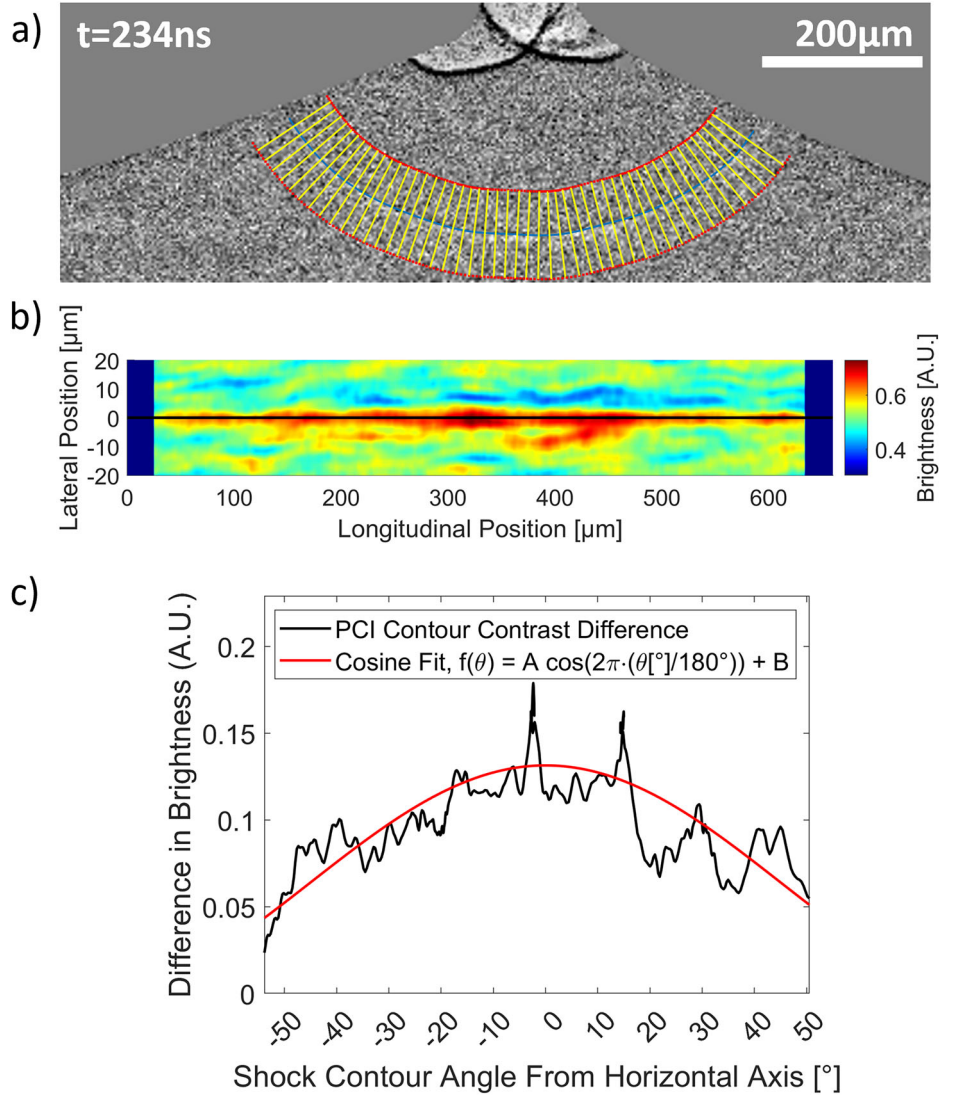
repetition rate⁵⁷⁻⁵⁹. This high event rate is particularly promising for machine learning applications; the eighty-five shock fronts cataloged in Fig. 3 could be used in the future to train a deep learning model for rapid analysis and computation of shock parameters, since it rapidly and stochastically queries a wide range of parameters (imaging delay time, shock shape, breakdown voltage, etc.). This advantage would also still hold for plasma-induced shock events in other media of interest. This avenue also has potential for observation of higher-order shock structure and non-uniformity. Future endeavors will focus on extending the XPCI sensitivity threshold for shock imaging while continuing to develop a quantitative analysis toolkit, for shock imaging as well as for more general HED and ICF applications.

Methods

Experimental setup details

See Fig. 1 for photographs of the experimental setup as installed at the APS and a diagram of the apparatus. The high-voltage circuit used in this work to generate the submerged spark discharge event is similar to those used in our prior work^{37,38}. An RC circuit was used to charge a 1nF capacitor, which was then triggered using an Nd:YAG ns-pulsed laser to breakdown across an air

Fig. 6 | Extraction and quantification of XPCI longitudinal shock contour. **a** Spline-fit shock contour extraction on the same XPCI frame from Fig. 4. **b** Instead of averaging all cutlines, in this case we plot them as a function of longitudinal position. **c** By taking an average of the lateral positions corresponding to the XPCI maxima ($-5 \mu\text{m}$ to $5 \mu\text{m}$) and minima ($5 \mu\text{m}$ to $15 \mu\text{m}$), the difference between these averages can then be plotted as a function of the shock contour angle; this plot is sensitive to the instrument function's elliptic anisotropy, causing the amplitude of this XPCI contour to have a cosine dependence on angle relative to the X-ray source.



spark gap⁶⁰, in series with a submerged spark gap within the imaging target. The resulting submerged spark event was therefore well-timed relative to the APS's X-ray timing systems. On average, applied voltage pulses were approximately 15 kV, with an estimated pulse energy of approximately 100 mJ released as plasma energy in the target, and instantaneous power reaches a maximum of roughly 2 MW; see Fig. 1 for voltage, current, power, and energy traces from a typical heptane spark discharge event.

Phase contrast imaging computational model derivation

The general form of the Fresnel-Kirchhoff diffraction integral for a two-dimensional sample and detector planes separated by a distance z can be expressed as follows:

$$g_{\text{out}}(x', y') = \frac{e^{2\pi iz/\lambda}}{i\lambda z} \int_{-\infty}^{\infty} \int_{-\infty}^{\infty} g_{\text{in}}(x, y) e^{\frac{i\pi}{\lambda z}((x'-x)^2 + (y'-y)^2)} dx dy \quad (5)$$

where $g_{\text{in}}(x, y)$ and $g_{\text{out}}(x', y')$ represent the complex-valued electric field at the sample and detector planes, respectively. The paraxial approximation $\sqrt{(x' - x)^2 + (y' - y)^2} \gg z$ has been applied, and $z = 46 \text{ cm}$ for the results presented in this work. For translationally symmetric samples oriented perpendicular to the optical axis, symmetry implies $g_{\text{in}}(x, y) = g_{\text{in}}(x)$ and $g_{\text{out}}(x, y) = g_{\text{out}}(x)$, enabling more efficient analytic

evaluation of the y -integral:

$$g_{\text{out}}(x') = \frac{e^{2\pi iz/\lambda}}{i\lambda z} \int_{-\infty}^{\infty} \int_{-\infty}^{\infty} g_{\text{in}}(x) e^{\frac{i\pi}{\lambda z}((x'-x)^2 + (y'-y)^2)} dx dy \quad (6)$$

$$= \frac{e^{2\pi iz/\lambda}}{i\lambda z} \int_{-\infty}^{\infty} g_{\text{in}}(x) e^{\frac{i\pi}{\lambda z}(x'-x)^2} dx \int_{-\infty}^{\infty} e^{\frac{i\pi}{\lambda z}(y'-y)^2} dy \quad (7)$$

$$= \frac{e^{2\pi iz/\lambda}}{\sqrt{i\lambda z}} \int_{-\infty}^{\infty} g_{\text{in}}(x) e^{\frac{i\pi}{\lambda z}(x'-x)^2} dx \quad (8)$$

The function $g_{\text{in}}(x)$ completely describes the sample plane and must be defined explicitly. We assume the pre-sample X-ray beam to be coherent, collimated, and in phase. If we normalize by g_{beam} , the post-sample beam electric field $g_{\text{in}}(x)$ can be expressed as $g_{\text{in}}(x) = g_{\text{beam}}(x)g_t(x) = g_t(x)$ where $g_t(x)$ is the following function for a curvilinear shock contour in heptane with a circular cross section:

$$g_t(x) = e^{-\frac{2ix}{\lambda}} \int \tilde{n}(x, z) dz \quad (9)$$

$$= \begin{cases} e^{\left[\frac{-2i\tilde{n}}{\lambda}w_{\text{heptane,ambient}} \cdot w_{\text{liq}}\right]}, & |x| > R \\ e^{\left[\frac{-2i\tilde{n}}{\lambda}w_{\text{heptane,ambient}} \cdot (w_{\text{liq}} - 2\sqrt{R^2 - x^2})\right]} \\ e^{\left[\frac{-2i\tilde{n}}{\lambda}w_{\text{heptane,post-shock}} \cdot (2\sqrt{R^2 - x^2})\right]}, & |x| \leq R \end{cases} \quad (10)$$

where $\tilde{n} = 1 - \delta - i\beta$ is the complex index of refraction of a given medium⁴⁵, R is the radius of the shock, w_{liq} is the thickness of the target cell (~ 6 mm in this work), and $x = 0$ is the centerline of the spark discharge event. The windows of the cell are made of 0.005" polyimide film which may be neglected for the purposes of this analysis. The indices of refraction for ambient heptane and for a higher density post-shock heptane region of density $\rho_{\text{heptane,post-shock}}$ are related via $\tilde{n}_{\text{heptane,post-shock}} = 1 - \frac{\rho_{\text{heptane,post-shock}}}{\rho_{\text{heptane,ambient}}}(\delta + i\beta)_{\text{heptane,ambient}}$

Data availability

Full-resolution imaging data presented via figures in this work is available to readers upon request, pending the consent of all authors. Any dissemination of additional related results and analysis methods not directly displayed herein is subject to LANL public release policies and restrictions, and is also contingent upon author consent.

Code availability

Similar to data availability, the code used to compute the simulation results presented in this work is available to readers upon request, pending the consent of all authors and subject to LANL public release policies and restrictions.

Received: 29 May 2024; Accepted: 25 February 2025;

Published online: 01 April 2025

References

- Kerby, J. The advanced photon source upgrade: A brighter future for x-ray science. *Synchrotron Radiat. N.* **36**, 26–27 (2023).
- Raimondi, P. et al. The extremely brilliant source storage ring of the european synchrotron radiation facility. *Commun. Phys.* **6**, 82 (2023).
- Rack, A. Hard x-ray imaging at esrf: Exploiting contrast and coherence with the new ebs storage ring. *Synchrotron Radiat. N.* **33**, 20–28 (2020).
- Tschentscher, T. Investigating ultrafast structural dynamics using high repetition rate x-ray FEL radiation at European XFEL. *Phys. J. Plus* **138**, 274 (2023).
- Galayda, J. N. The lcls-ii: A high power upgrade to the lcls. *9th International Particle Accelerator Conference* (2018).
- Zylstra, A. B. et al. Experimental achievement and signatures of ignition at the national ignition facility. *Phys. Rev. E* **106**, 25202 (2022).
- Zhao, C. et al. Real-time monitoring of laser powder bed fusion process using high-speed x-ray imaging and diffraction. *Sci. Rep.* **7**, 3602 (2017).
- Montgomery, D. S. Invited article: X-ray phase contrast imaging in inertial confinement fusion and high energy density research. *Rev. Sci. Instrum.* **94**, 021103 (2023).
- Hatfield, P. W. et al. The data-driven future of high-energy-density physics. *Nature* **593**, 351–361 (2021).
- Ram, O. & Sadot, O. Implementation of the exploding wire technique to study blast-wave-structure interaction. *Exp. Fluids* **53**, 1335–1345 (2012).
- Dattelbaum, D. M., Ionita, A., Patterson, B. M., Branch, B. A. & Kuettner, L. Shockwave dissipation by interface-dominated porous structures. *AIP Adv.* **10**, 075016 (2020).
- Sechrest, Y., Campbell, C., Tang, X., Staack, D. & Wang, Z. High-speed imaging of transition from fluid breakup to phase explosion in electric explosion of tungsten wires in air. *Appl. Phys. Lett.* **117**, 10–15 (2020).
- Im, K.-S. et al. Interaction between supersonic disintegrating liquid jets and their shock waves. *Phys. Rev. Lett.* **102**, 074501 (2009).
- O'Malley, S. M. et al. Nanosecond laser-induced shock propagation in and above organic liquid and solid targets. *Chem. Phys. Lett.* **615**, 30–34 (2014).
- Magaletti, F., Marino, L. & Casciola, C. Shock wave formation in the collapse of a vapor nanobubble. *Phys. Rev. Lett.* **114**, 064501 (2015).
- Perkins, L. J., Betti, R., LaFortune, K. N. & Williams, W. H. Shock ignition: A new approach to high gain inertial confinement fusion on the national ignition facility. *Phys. Rev. Lett.* **103**, 045004 (2009).
- Saiki, T. et al. Single-shot optical imaging with spectrum circuit bridging timescales in high-speed photography. *Sci. Adv.* **9**, eadj8608 (2024).
- Hwang, H. et al. Subnanosecond phase transition dynamics in laser-shocked iron. *Sci. Adv.* **6**, eaaz5132 (2024).
- Brown, S. B. et al. Direct imaging of ultrafast lattice dynamics. *Sci. Adv.* **5**, eaau8044 (2024).
- Kim, T., Liang, J., Zhu, L. & Wang, L. V. Picosecond-resolution phase-sensitive imaging of transparent objects in a single shot. *Sci. Adv.* **6**, eaay6200 (2024).
- MacNider, B. et al. In situ measurement of damage evolution in shocked magnesium as a function of microstructure. *Sci. Adv.* **9**, eadi2606 (2024).
- Ruby, J. J. et al. Constraining physical models at gigabar pressures. *Phys. Rev. E* **102**, 53210 (2020).
- Tang, M., Wu, Y. & Wang, H. Experimental investigation on hypersonic shock-shock interaction control using plasma actuator array. *Acta Astronautica* **198**, 577–586 (2022).
- Seshadri, P. K. & De, A. Investigation of shock wave interactions involving stationary and moving wedges. *Phys. Fluids* **32**, 096110 (2020).
- R, A. K. & Pathak, V. Shock wave mitigation using zig-zag structures and cylindrical obstructions. *Def. Technol.* **17**, 1840–1851 (2021).
- Zhao, W. et al. Design of shock wave attenuation effects on multi-impedance-matched laminated composites. *J. Mater. Res. Technol.* **23**, 5846–5860 (2023).
- Glenzer, S. H. et al. Symmetric inertial confinement fusion implosions at ultra-high laser energies. *Science* **327**, 1228–1231 (2010).
- Vassholz, M. et al. Pump-probe x-ray holographic imaging of laser-induced cavitation bubbles with femtosecond fel pulses. *Nat. Commun.* **12**, 3468 (2021).
- Yanuka, D. et al. Multi frame synchrotron radiography of pulsed power driven underwater single wire explosions. *J. Appl. Phys.* **124**, 153301 (2018).
- Barbato, F. et al. Quantitative phase contrast imaging of a shock-wave with a laser-plasma based x-ray source. *Sci. Rep.* **9**, 18805 (2019).
- Vanraes, P. & Bogaerts, A. Plasma physics of liquids—a focused review. *Appl. Phys. Rev.* **5**, 031103 (2018).
- Taylor, N. D., Fridman, G., Fridman, A. & Dobrynin, D. Non-equilibrium microsecond pulsed spark discharge in liquid as a source of pressure waves. *Int. J. Heat. Mass Transf.* **126**, 1104–1110 (2018).
- Wang, K. et al. Co2-free conversion of fossil fuels by multiphase plasma at ambient conditions. *Fuel* **304**, 121469 (2021).
- Wang, K. et al. Electric fuel conversion with hydrogen production by multiphase plasma at ambient pressure. *Chem. Eng. J.* **433**, 133660 (2022).
- Akiyama, H. & Akiyama, M. Pulsed discharge plasmas in contact with water and their applications. *IEEJ Trans. Electr. Electron. Eng.* **16**, 6–14 (2021).
- Furusato, T., Sasaki, M., Matsuda, Y. & Yamashita, T. Underwater shock wave induced by pulsed discharge on water. *J. Phys. D: Appl. Phys.* **55**, 115203 (2022).
- Akhter, M., Mallams, J., Tang, X. & Staack, D. Underwater plasma breakdown characteristics with respect to highly pressurized drilling applications. *J. Appl. Phys.* **129**, 183309 (2021).
- Campbell, C. et al. Ultrafast x-ray imaging of pulsed plasmas in water. *Phys. Rev. Res.* **3**, L022021 (2021).

39. E. N. A. of Sciences and Medicine, *Fundamental Research in High Energy Density Science* (The National Academies Press, 2023).
40. Borland, M. et al. Aps storage ring parameters. <https://ops.aps.anl.gov/SRparameters/SRparameters.html> (2024).
41. Taylor, G. I. The formation of a blast wave by a very intense explosion i. theoretical discussion. *Proc. R. Soc. Lond. Ser. A. Math. Phys. Sci.* **201**, 159–174 (1950).
42. Grun, J. et al. Instability of Taylor-Sedov blast waves propagating through a uniform gas. *Phys. Rev. Lett.* **66**, 2738 (1991).
43. Lin, S. C. Cylindrical shock waves produced by instantaneous energy release. *J. Appl. Phys.* **25**, 54–57 (1954).
44. Barbastathis, G., Sheppard, C. & Oh, S. B. 2.71 optics, lecture 15. *MIT OpenCourseWare*, <https://ocw.mit.edu>.
45. Henke, B. L., Gullikson, E. M. & Davis, J. C. X-ray interactions: photoabsorption, scattering, transmission, and reflection at $e=50$ – 30000 eV, $z=1$ – 92 . *Atomic Data and Nuclear Data Tables* **2** (1993).
46. Span, R. & Wagner, W. Equations of state for technical applications. ii. results for nonpolar fluids. *Int. J. Thermophys.* **24**, 41–109 (2003).
47. Schropp, A. et al. Imaging shock waves in diamond with both high temporal and spatial resolution at an xfel. *Sci. Rep.* **5**, 11089 (2015).
48. Blum-Sorensen, C. J. et al. Phase contrast x-ray imaging of the collapse of an engineered void in single-crystal hmx. *Propellants, Explosives, Pyrotechnics* **47**, e202100297 (2022).
49. John, J. E. A. & Keith, T. G. *Gas Dynamics* (Pearson Prentice Hall, 2006).
50. Crossfield, I., Hughes, S. & E., M. 8.901 astrophysics i lecture notes. *MIT OpenCourseWare* (2019).
51. Henderson, L. R. *CHAPTER 2 - General Laws for Propagation of Shock Waves Through Matter*, 143–183 (Academic Press, 2001).
52. Costanzo, F. A. Underwater explosion phenomena and shock physics. In Proulx, T. (ed.) *Structural Dynamics, Volume 3*, 917–938 (Springer New York, 2011).
53. Hess, G. R. Plasma driven water shock. <https://oa.mg/work/10.21236/ada305572> (1996).
54. Ishii, K. & Watanabe, N. Shock wave generation by collapse of an explosive bubble in water. *Proc. Combust. Inst.* **37**, 3653–3660 (2019).
55. Wang, H.-C. et al. Roles of underwater explosion bubble accelerating expansion cut-off state in bubble dynamics and energy output. *J. Appl. Phys.* **132**, 194704 (2022).
56. Hettel, R. Status of the aps-u project*. *Proceedings of IPAC2021 7–12* (2021).
57. Chu, F. et al. Experimental measurements of ion diffusion coefficients and heating in a multi-ion-species plasma shock. *Phys. Rev. Lett.* **130**, 145101 (2023).
58. Gao, L. et al. Hot spot evolution measured by high-resolution x-ray spectroscopy at the national ignition facility. *Phys. Rev. Lett.* **128**, 185002 (2022).
59. Nora, R. et al. Gigabar spherical shock generation on the omega laser. *Phys. Rev. Lett.* **114**, 045001 (2015).
60. Larsson, A., Yap, D., Au, J. & Carlsson, T. E. Laser triggering of spark gap switches. *IEEE Trans. Plasma Sci.* **42**, 2943–2947 (2014).

Acknowledgements

This work has been approved for public release, LANL LA-UR-24-24881. This research used resources of the Advanced Photon Source, a U.S. DOE

Office of Science user facility operated by Argonne National Laboratory under Contract No. DE-AC02-06CH11357. LANL work performed under the auspices of the U.S. DOE by Triad National Security, LLC, Contract No. 89233218CNA000001.

Author contributions

C. Campbell and M. Akhter were equally responsible for experiment design, planning, and execution. Data analysis and manuscript writing by C. Campbell. S. Clark and K. Fezzaa are affiliated with the user facility where this work was performed, and both assisted with facility operation and imaging. D. Staack supported this work in a mentorship role, contributing equipment as well as graduate research assistant time/travel. Z. Wang also supported this work in a mentorship role, and was responsible for acquiring the required user facility beamtime.

Competing interests

The authors declare no competing interests.

Additional information

Supplementary information The online version contains supplementary material available at <https://doi.org/10.1038/s42005-025-02021-4>.

Correspondence and requests for materials should be addressed to Christopher S. Campbell or Zhehui Wang.

Peer review information: *Communications Physics* thanks the anonymous reviewers for their contribution to the peer review of this work. A peer review file is available.

Reprints and permissions information is available at <http://www.nature.com/reprints>

Publisher's note Springer Nature remains neutral with regard to jurisdictional claims in published maps and institutional affiliations.

Open Access This article is licensed under a Creative Commons Attribution-NonCommercial-NoDerivatives 4.0 International License, which permits any non-commercial use, sharing, distribution and reproduction in any medium or format, as long as you give appropriate credit to the original author(s) and the source, provide a link to the Creative Commons licence, and indicate if you modified the licensed material. You do not have permission under this licence to share adapted material derived from this article or parts of it. The images or other third party material in this article are included in the article's Creative Commons licence, unless indicated otherwise in a credit line to the material. If material is not included in the article's Creative Commons licence and your intended use is not permitted by statutory regulation or exceeds the permitted use, you will need to obtain permission directly from the copyright holder. To view a copy of this licence, visit <http://creativecommons.org/licenses/by-nc-nd/4.0/>.

© The Author(s) 2025